CrystEngComm

Accepted Manuscript

ROYAL SOCIETY OF CHEMISTRY

www.rsc.org/crystengcomm

CrystEngComm

ARTICLE

Single crystal form induced diversity interface structures in TiO_2 (B)/anatase dual-phase nanocomposites

Received 00th January 20xx,
Accepted 00th January 20xx

DOI: 10.1039/x0xx00000x

www.rsc.org/

Jie Sun[a, c, d, *], Yimin Lei[b, c, d], Hongwei Liu[d], S. P. Ringer[d, e], Zongwen Liu[c, *]

The growth morphologies of two types of single crystal forms the induced multiple interface structures in TiO_2 (B)/anatase nanofibers were investigated by means of scanning and transmission electron microscopy. It is suggested that both single crystal forms have the same lath shaped morphology with the only differences of size and thickness. By calculating 4 parameters which may affect the growth of selected facets from the perspective of crystallography, the competition mechanism between two single crystal forms has been interpreted successfully. Moreover, different interface structures induced by different single crystal forms of TiO_2 (B) were also confirmed during the phase transformation from TiO_2 (B) to anatase. Through the analysis of these interface structures, it is believed that the interface of $(001)_{TB}//(100)_{TA}$ contain larger nanotunnels than that in $(100)_{TB}//(100)_{TA}$ interface. These nanotunnels are considered more suitable for lithium ions intercalation and deintercalation in the application of Li^+ batteries. Moreover, the existence of these coherent interfaces is favorable to the carrier transfer during the photocatalytic process. The results of this work provide a potential idea to prepare the TiO_2 nanocrystals with multi-purposes.

1. Introduction

TiO_2 is one of the most popular materials in the field of photocatalyst.[1-4] Available in four common polymorphs (TiO_2 (B), anatase, rutile and brookite), TiO_2 have been widely developed into nanostructures or thin films to utilize at variety areas such as solar cells, [5, 6] lithium ion storage[7] and biological use.[8] Besides the usage of absorption and catalyst like anatase and rutile,[9-11] TiO_2 (B) (TB) is also found very suitable for lithium ions insertion under nanometer size due to its open structure which can allow small ions to pass through.[12, 13] The existence of these "nanotunnels" in TB is the decisive factor to the passing rate of lithium ions. However, the single crystal form (SCF), which has been determined during the crystal growth process, will lead to the formation of different crystal morphology and structures and thus, affect the quantity and shape of nanotunnels inside the crystals. Considering the widely used TB nanofibers, the SCF belongs to simple planar groups, for example, (100) or (001), each of which is enclosed by a pair of parallel facets. For the common TB nanofibers grown by hydrothermal reaction, the growth direction is normally along $[010]$ because the system energy is the lowest under this growth behaviour. This suggests the most probable SCFs for TB are $(001\}$ and $\{100)$† with similar larger d-spacing (0.6237 nm for $(001)_{TB}$ and 0.5826 nm for $(200)_{TB}$). Here, the cell parameters of TB are *a*=1.2208 nm, *b*=0.3749 nm, *c*=0.6535 and *β*=107.36°, which are taken from the XRD database (JCPDS file number 46-1238). In fact, these two SCFs have been observed and analyzed in previous research works.[14] However, the coexistence and competition mechanism between different SCFs of TB are still mystery up to now. These two aspects will definitely affect the internal structure of the nanofibers including the shape and quantity of nanotunnels at the interface region.

On the other hand, interface plays a very important role in the application of TiO_2 photocatalysts as the electrons will flow from one phase to another when their band-gap and work functions are different.[15-18] Therefore, the synthesis of nanocomposites with different TiO_2 polymorphs to enhance the photocatalytic response and activity is one of the typical way in recent research works.[19, 20] Since there are two SCFs of TB coexistent during the crystal growth process, it is essential to figure out the differences of the interface structures induced by different SCFs. This is quite important to the charge transfer as well as the size and quantity of nanotunnels. Normally, the best choice for the anode of lithium ion batteries is pure TB phase if interface cannot maintain or expand the nanotunnels. For the case of TB, the C sites lie in the open channel along the b-axis is the most easily occupied

[a.] School of Materials Science and Engineering, Shaanxi Normal University, Xi'an 710119, P. R. China.
[b.] School of Advanced Materials and Nanotechnology, Xidian University, Xi'an 710126, P. R. China.
[c.] School of Chemical and Biomolecular Engineering, The University of Sydney, NSW 2006, Australia.
[d.] Australian Centre for Microscopy & Microanalysis, The University of Sydney, NSW 2006, Australia.
[e.] School of Aerospace, Mechanical and Mechatronic Engineering, The University of Sydney, NSW 2006, Australia.

‡ Electronic Supplementary Information (ESI) available: [The TEM BF images and corresponding SAED patterns for counting the species of SCFs for TB nanofibers can be found in the supplementary materials. Also, the HRTEM image illustrating the twins and anti-phase boundaries in TB nanofibers is also shown in the supplementary materials.]. See DOI: 10.1039/x0xx00000x

position for lithium ions.[12, 21] Therefore, it can be speculated that the transport of these ions may be blocked if the parent and new phase do not exhibit a b-axis parallel orientation relationship (OR). Although the main (010) parallel OR in TB/TA system has been confirmed,[22, 23] the diversity interface structures with incoherent status are stilled observed in our previous research works.[24] Hence, the existence of these incoherent interfaces is speculated to prevent the intercalation and deintercalation of the lithium ions. On the contrary, the photocatalytic properties require interfaces to enhance the charge transfer based on the band alignment between different TiO_2 polymorphs.[10, 25, 26] In this case, the fabrication of TB/TA nanofibers with multiple purposes is feasible if the OR between TB and TA can be controlled to make the nanotunnels expanded at the interface region.

The structures of TB/TA interfaces have been confirmed to have a major OR of $[001]_{\mathrm{TB}}//[100]_{\mathrm{TA}}$.[22, 23] However, the results here are all based on the (001) SCF although it has never been pointed out in the related references. For $\{100)$ SCF, the OR and lattice correspondence are considered to be different. As mentioned above, our recent studies indicates the interfaces between TB and TA may have different ORs apart from $[001]_{\mathrm{TB}}//[100]_{\mathrm{TA}}$ when the calcination temperature reached 700 °C.[24] The diversity of TB/TA interface structures will also affect the photocatalytic properties as different structures are speculated to have different charge transfers across the interfaces. Therefore, it is quite essential to investigate and interpret the different TB/TA interface structures induced by different SCFs in order to deep understand the variation mechanism of the photocatalytic properties.

The purpose of this work is dedicated to interpret the crystallographic features as well as the competition mechanism of two SCFs in TB nanofibers. Meanwhile, the formation of multiple ORs between TB and TA induced by different SCFs are also explained in detail. Furthermore, through the analysis of TB/TA interface models with different lattice correspondence, the lithium ion transport through different interface structures were also discussed. This work also provided a possible concept to synthesis the TB nanofibers with multiple purposes.

2. Experimental

The TB nanofibers used in this study were synthesized from $H_2Ti_3O_7$ nanofibers. To achieve the goal, $H_2Ti_3O_7$ nanofibers were first prepared by a hydrothermal reaction between a concentrated NaOH solution and an inorganic titanium salt.[27] In detail, $TiOSO_4{\cdot}xH_2O$ (10.7 g) was dissolved into water (80 mL) and stirred until clear. Then the resultant $TiOSO_4$ solution was mixed with NaOH solution (100 mL, 15m) while stirring. The mixture was then transferred into a 200 mL Teflon-lined stainless steel autoclave and kept at a temperature (T_h) between room temperature and 200 °C for 48 h to obtain titanate precipitates through a hydrothermal reaction. The white precipitates in the autoclaved mixture were collected by centrifugation and washed with distilled water five times by dispersing the wet cake into water (100 mL) and recovering the solid by centrifugation. The sodium titanate product was then neutralized using HCl solution (0.1 M) and washed with water to remove most of the sodium ions. The final product was $H_2Ti_3O_7$ nanofiber. Pure TB nanofigers can be obtained by calcining the $H_2Ti_3O_7$ nanofibers in air under 400 °C for 2 hours. The detailed phase transformation and dehydration mechanism from $H_2Ti_3O_7$ to TB can be found in our previous work.[28] The JSM-7610F scanning electron microscope (SEM) was employed to investigate the growth morphology of the two SCFs of TB nanofibers. To obtain the interfaces between TB and TA, some TB nanofibers were continued to heat at 650 °C for 1 hour to promote the phase transformation from TB to TA. Both the nanofibers with pure TB and mixed phase were dispersed on a copper grid with holy carbon film for TEM observation which was carried out on JEM-2200FS and JEM-3000F filed emission TEM. The series tilting experiment was carried out to determine the most suitable viewing directions to observe the morphology of the nanofibers with different SCFs. To achieve the goal, an X-Y type double-tilt TEM specimen holder with the tilting limit of TX=TY=±30° was employed for the experiment.

3. Results

3.1 The morphologies of two SCFs of TB nanofibers

Figure 1 shows the SEM results illustrating the growth morphology of TB nanofibers with different SCFs. Seeing from Fig. 1 (a), it can be seen that the as-synthesized TB nanofibers have a typical morphology of 1D nanocrystals. The size distribution of these nanofibers is somewhat nonuniform. The width of the nanofibers is ranging from 40-600 nm while the length is between 0.5 and 12.0 μm. Through careful analysis on Fig. 1 (a), it is noticed that there are two types of nanofibers with similar morphology coexisted in the system. The first type is flatter with larger exposed facets while the second type is thinner and longer. We believe that the two types of nanofibers can be ascribed to the two SCFs in TB, as illustrated in the figure. Moreover, the SCF with larger diameter is found dominant in quantity during the entire experiment. This can be attributed to the competition of two SCFs in TB and will be discussed in Section 4.1. By increasing the magnification, it is possible to measure the detailed diameter of the two types of SCFs, as shown in Fig. 1 (b) and (c). Seeing from the figures, it is found that the sizes of the two SCFs are quite different. For the first type with larger facets, the diameter of the nanofibers is also larger (mostly > 140 nm). While for the second type, the size of most nanofibers are at the range from 40nm to 140 nm. This interesting results can be attributed to the different exposed facets of the two SCFs. Through a close-up viewing of one nanofibers which taken from the red rectangle in Fig. 1 (b), the lath shape morphology can be observed clearly, as indicated in Fig. 1 (d). The results obtained here are consistent with the previous observations.[14]

In order to further investigate the detailed crystallographic features of the two SCFs in TB, TEM experiment was carried

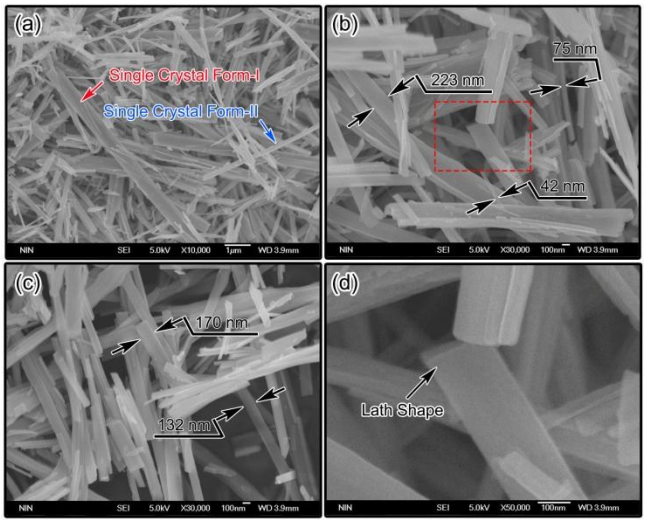

Fig. 1 The SEM overview images (a) of the as-synthesized TB nanofibers. The enlarged images (b) and (c) indicate different diameters of the two SCFs. Both SCFs are found to have the lath shaped morphology with the only difference of size and thickness according to (d) which was taken from the red rectangle area in (b).

out under different viewing directions. Fig. 2 (a) and (b) illustrate the TEM bright field (BF) images of two types of SCFs in TB nanofibers. The corresponding selected area electron diffraction (SAED) patterns are shown in Fig. 2 (c) and (d) respectively. It is noted that plenty of "wrinkles" like contrast will appear for both SCFs when tilting the samples to the zone axes which contain strong reflections of (020). This phenomenon, which can be utilized to determine whether a certain zone axis is reached, is only found in $H_2Ti_3O_7$ and TB nanofibers. The reasons for this can be concluded to the following two aspects. Firstly, the $[010]$ growth directions (also the normal direction of (020)) of TB will lead to the relatively strong diffraction intensity for (020) plane due to the 1D structure and lath shape morphology. Secondly, the plenty of defects in TB inherited from the hydrothermal synthesized $H_2Ti_3O_7$ nanofibers will give additional contrast to the TEM BF images. These "wrinkles" like contrast which are similar to the equal inclination fringes can only show one pair of fringes in such 1D structure, which is quite different from that in the bulk materials. By comparison, the observed contrast in TA is quite different. It is noticed that the surface of TA phase transformed from TB exhibit a smooth status. The strong diffraction intensity of (011) becomes the main contribution to the contrast of TA. Therefore, it is a intuitive method to distinguish TB and TA phase through the differences in the diffraction contrast in TEM BF images.

For the two types of SCFs in TB nanofibers, the most suitable viewing directions should be $[100]$ and $[001]$, which is also the method to distinguish different SCFs in present work. It is noted that the lattice spacing of $(h00)$ and $(00l)$ are very close to each other (for instance 0.6237 nm for (001) and 0.5826 nm for (200)). In this case, the obvious differences in the SAED patterns are the existence of (110) and $(\bar{1}10)$ spots in (001) SCF as the $(01l)$ series of spots are all forbidden reflections in TB when viewing along $[100]$ direction. Combined with the different lattice spacing between $(h00)$ and $(00l)$ spots with high index, it is possible to distinguish the two SCFs in TB nanofibers.

The thickness maps of the two types of SCFs in TB are also collected along $[100]$ and $[001]$ zone axis for $\{100)$ and $(001\}$ SCF to further establish the detailed crystallographic morphology models respectively. The profile line chart was shown in Fig. 2 (e) and (f). It is noted that the surface of TB nanofibers are not smooth for both SCFs, which confirms the existence of defects at the surface. In addition, the mean thicknesses illustrated by blue dashed lines are found to be 37.89 nm and 30.83 nm for $\{100)$ and $(001\}$ SCFs. As the SCF of TB with 1D nanostructure belongs to the simple planar group in monoclinic structure, it can be speculated that the morphologies of nanofibers are lath shape based on the SEM results. However, the arc shaped thickness curves for both SCFs do not meet the speculations. This may be due to the inappropriate viewing directions for capturing of thickness maps as there are 17.3° and 18.1° deviation from $[100]$ to $(100)^*$ and $[001]$ to $(001)^*$ for TB respectively. Here $(100)^*$

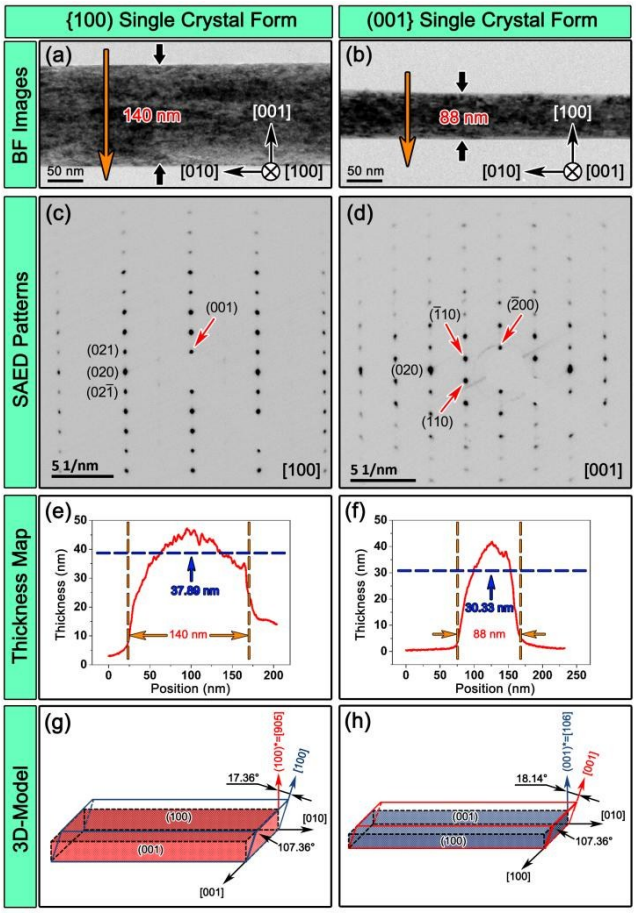

Fig. 2 The TEM BF images (a), (b) and corresponding SAED patterns (c), (d) for the two types of TB SCFs indicate two different zone axes. The orange arrows in (a) and (b) represent the position of carrying out thickness map experiments. The appearance of (110) and $(\bar{1}10)$ spots in the SAED patterns taken along $[001]$ zone axis is the main difference to distinguish the two SCFs. The thickness profiles for $\{100)$ (e) and $(001\}$ (f) SCF suggest the similar morphologies. The schematic drawings with detailed crystallographic features of two SCFs are also illustrated (g) and (h). A 17.36° and 18.14° angle differences between the plane normal and direction with the same index are also illustrated in the images.

and $(001)^*$ represent the normal directions of (100) and (001) plane. As the viewing directions in this study were determined by monitoring the SAED patterns, such difference will lead to the oblique projection of the nanofibers, and further generating the arch shaped curves. Moreover, due to the tilting limit of the TEM sample holder, it is difficult to have the incident beam directions along $(100)^*$ or $(001)^*$ in our experiment.

Based on the results and discussions above, the schematic images illustrating the detailed crystallographic features of two SCFs can be drawn, as shown in Fig. 2 (g) and (h). Here, the red and blue parallelepipeds illustrate the actual lath morphology of $\{100)$ and $(001\}$ SCFs, while the blue and red frame outside the parallelepipeds indicate the crystal cell enclosed by 3 basal axes. As the viewing directions for the two types of SCFs are set to be $[100]$ and $[001]$, the observed morphology is not to be the standard parallelepiped due to the difference of β angle in monoclinic structures, which are also revealed in the thickness map profiles. In addition, the directions which perpendicular to (100) and (001) in TB are calculated to be $[905]$ and $[106]$ respectively, 17.36° and 18.14° away from $[100]$ and $[001]$ directions. These angle deviations on the viewing directions are the reason of arch shaped curves shown in the thickness map results. Furthermore, the minor facets are also marked as (001) and (100) for $\{100)$ and $(001\}$ SCFs respectively in order to illustrate the morphology intuitively. But these two planes have limited area and effect in the practical application.

By carrying the above method to distinguish the two types of SCFs, we have recorded the different diameters of several nanofibers accurately by TEM to illustrate the relationship between the size and the SCF type, eight of which has been summarized in Table 1. Consistent with the SEM results, $\{100)$ SCF normally have larger diameter compared with $(001\}$ SCF. This can be attributed to the smaller d-spacing of $\{100)$ planes which may lead to a larger growth speed. The TEM BF images and corresponding SAED patterns for the nanofibers listed in Table 1 can be found in the supplementary materials‡ of this paper. Moreover, $\{100)$ SCF is proved to be dominant again among all the nanofibers, indicating $\{100)$ SCF win the SCF competition during the crystal growth process.

Table 1 The diameters and corresponding SCF of TB nanofibers.

No.	Diameter (nm)	SCF
1	47	$(001\}$
2	73	$(001\}$
3	88	$(001\}$
4	133	$(001\}$
5	140	$\{100)$
6	176	$\{100)$
7	210	$\{100)$
8	216	$\{100)$

3.2 Determination of the most suitable viewing directions of TB nanofibers

Suitable viewing direction is essential in TEM experiments when analyze the detailed crystallographic features of TB nanofibers. Owing to the low structure symmetry and the size effect of TB nanofibers, the reciprocal points are normally elongated, which will relax the diffraction conditions, leading to the appearance of some spots even the incident beam is not strictly along a certain zone axis. Meanwhile, the growth direction of TB nanofibers prepared by hydrothermal method is mainly along $[010]$ direction, leading to the existence of strong (020) reflection in the SAED patterns. Therefore, previous researches on TB nanofibers normally regard the SAED patterns with the coexisted (020) and $(h0l)$ or $(\bar{h}0l)$ spots as the zone axis of $[100]$ and $[001]$ respectively.[23, 29] In fact, these zone axes are normally with the index of $[u0\bar{w}]$ or $[u0w]$ respectively. The spots representing $(00l\}$ or $\{h00)$ will appear sometimes due to the size effect of TB nanofibers.

In order to determine the most suitable viewing directions of TB nanofibers, the series tilting experiment was performed. The $\{100\}$ SCF was chosen as an example to carry out the tilting experiment. The tilting range for the holder is from -30° to +30° for both along X and Y directions. Fig. 3 (a)-(g) summarized the SAED patterns of 7 viewing directions (VDs) for TB nanofibers grown along $[010]$ direction. Each SAED pattern was taken at almost the same place of the nanofiber, which can be confirmed from the existence of equal inclination fringes from BF images. The TX and TY values illustrated in the image of each VD are recorded directly from TEM goniometer system. The tilting from VD1 to VD6 is along the normal direction of (020), which has been marked with green circle in each figure. In addition, $(00l\}$ series of spots were keeping bright during the tilting from VD1 to VD7. The actual angle values between every two VDs shown near the blue arrows are estimated through the following equation:

$$\cos\theta \approx \cos\Delta\mathrm{TX}\cos\Delta\mathrm{TY} \quad (1)$$

Here ϑ represents the actual orientation differences between two VDs. ΔTX and ΔTY indicate the TEM recorded angle differences along *x* or *y* axes between two VDs. It is worth to mention that Eq. (1) is not the strictly accurate formula. Therefore, the nearby zone axes besides each VD are also taking into consideration to help the indexing of SAED patterns. Moreover, the calculated viewing directions are normally illustrated by fractional indexing as it is quite difficult to precise control every VD parallel to a certain zone axis during the experiment.

To start, the sample was first tilt to $[100]$ zone axis with the SAED patterns similar to Fig. 2 (c). It is worth to mention that there are some impurities in the nanofiber which contribute the weak spots between $(02l)$ and $(00l)$ series of spots. This can also be found at some other VDs such as VD2 and VD6. When tilting along $[010]$ axis for 4.84°, the spots representing (001) and (021) are still visible, indicating the viewing direction is not far away from $[100]$ zone axis. The calculated viewing direction is $[1.32, 0, \overline{0.19}]$ through Eq. (1). The nearest zone axis around VD2 is found to be $[60\bar{1}]$, which is illustrated at the lower right corner in Fig. 3 (h). This phenomenon is very common in TEM experiments because the strong reflections are still visible when the deviation of incident beam directions from the zone axis does not exceed ±5°. The $(00l\}$ series of

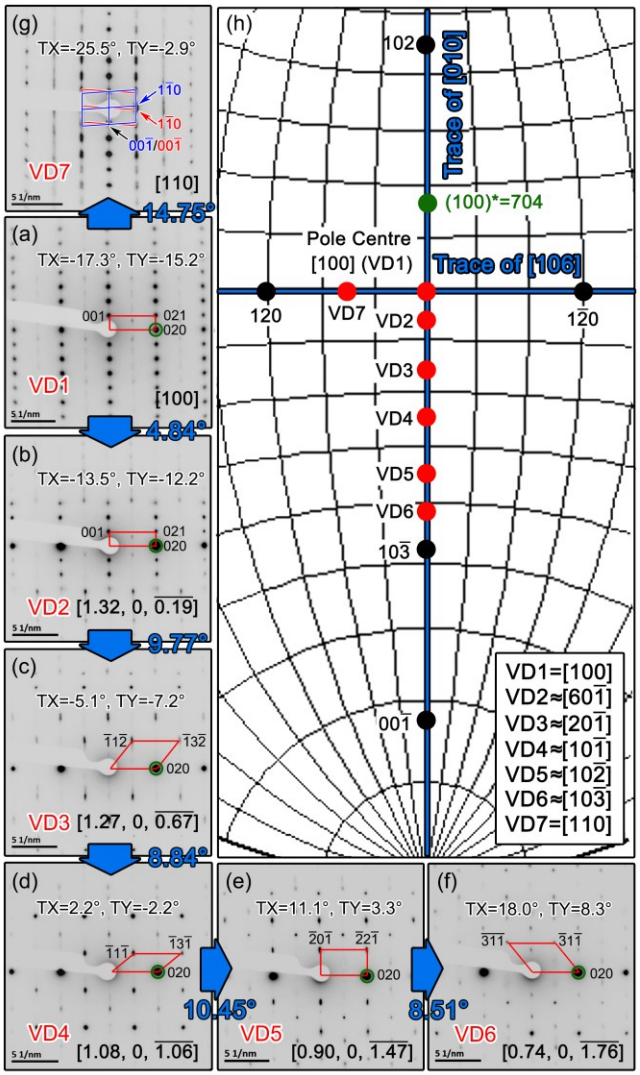

Fig. 3 The series tilting procedure on TB $\{100\}$ SCF nanofibers with the initial VD of $[100]$. The tilting was carried out along $[010]$ axis to reach VD2 to VD6 (b)-(f) and $[106]$ axis to reach VD7 (g). The (020) spots marked with green circles were keeping strong during the tilting. Typical mirror twinning features with the twin plane of (001) in TB nanofibers can be seen from the SAED patterns taken along $[110]$ zone axis. The blue and red indexing characters indicate matrix and twin respectively. Moreover, the crystallographic relationship of all VDs is illustrated in the stereographic projection of vectors (h). The green spots indicate the unapproachable position of normal direction of (100) due to the tilting limit of TEM.

spots disappeared after tilting for another 9.77° to VD3. At this stage, the zone axis is close to $[20\bar{1}]$. Continue tilt the sample along $[010]$ axis for 8.84°, 10.45° and 8.51°, VD4-6 can be obtained with the zone axes close to $[10\bar{1}]$, $[10\bar{2}]$ and $[10\bar{3}]$ respectively. For VD7, the tilting axis and angle are set to be the normal direction of (001) and 14.75°. Besides VD1 and VD7, the (020) spots are found very strong for the other 5 VDs, indicating these VDs are away from the closed-packed or near close-packed viewing directions.

By indexing the SAED pattern in Fig. 3 (g), the twin features can be obtained by perform a reflection operation with the mirror plane of (001). The index for matrix and twin is illustrated with blue and red characters. The HRTEM images were also taken under this viewing direction to illustrate the detailed structure of the extended defects. The existence of anti-phase boundary parallel to $(1\bar{1}0)$ plane can also be confirmed. Detailed images of the extended defects in TB nanofibers can also be found in the supplementary materials‡ of this paper. The extended defects found here is compliance with the previous research works.[14] Finally, the VDs involved here are all projected in the stereographic projection of vectors (Fig. 3 (h)). Two traces of $[010]$ and $[106]$ shown in the figure reveal the different rotation axes. It is worth to mention that $[106]$ is the normal direction of (001) plane. Therefore, it is reasonable that the orientations located on the trace of $[106]$ are all suitable directions to observe the twins in TB as $\{00l\}$ series of planes can always be seen. Moreover, the normal direction of (100) plane is close to the direction of $[704]$, which is 17.8° away from $[100]$ zone axis (green spots in Fig. 3 (h)). For the collection of thickness map, this direction is the most suitable zone axis as the nanofiber will be in the orthographic projection state. However, due to the specimen tilting limit, this orientation is difficult to achieve in our experiment. Therefore, it is reasonable that the thickness maps shown in Fig. 2 have gradual edges because the nanofibers are not in an edge-on position.

3.3 Diversity interface structures in TB/TA nanofibers induced by different SCFs.

After calcining the TB nanofiber at 650 °C for 1 hour, the interface structures between TB and TA were observed for both SCFs, as shown in Fig. 4 (a) and (b). It is noted that the interfaces are not strictly parallel to a certain lattice plane, indicating the release of internal stress is almost finished. At the beginning of the phase transformation, we have also found that the interfaces between TB and TA are very smooth. These interfaces are normally parallel to $(001)_{TB}$ for $\{100\}$ SCF (The results are not shown). However, no such initial interfaces can be found in $\{001\}$ SCF. The reason for this may be due to the different surface energies of the two SCFs with different facets. When seeing from the HRTEM images shown in Fig. 4 (c) and (d) for $\{100\}$ and $\{001\}$ SCFs, steps and kinks are found located along the interfaces, suggesting a typical edge mechanism of the phase transformation process from TB to TA. In addition, no obvious dislocations or stacking faults can be found, indicating a fully coherent status of the interfaces. From the inset FFT images, it is found that TA has the zone axis of $[100]$ for both SCFs, while TB has the incident beam directions along $[100]$ and $[001]$ for $\{100\}$ and $\{001\}$ SCF respectively. The existence of (110) and $(1\bar{1}0)$ spots in the FFT image of TB with $\{001\}$ SCF is the main difference compared with $\{100\}$ SCF. In addition, (020) spots keep overlapping for both SCFs according to the similar d-spacing of $(020)_{TB}$ and $(020)_{TA}$. Therefore, two types of orientation relationships can be obtained as follows:

$$[001]_{TB}//[001]_{TA}, (010)_{TB}//(010)_{TA}$$
$$[100]_{TB}//[001]_{TA}, (010)_{TB}//(010)_{TA} \quad (2)$$

The IFFT images shown in Fig. 4 (e) and (f) illustrate the detailed structures. The interfaces for both $\{100\}$ and $\{001\}$ SCFs are found parallel to $(001)_{TB}$ and $(100)_{TB}$ respectively. The detailed crystallographic features of the interfaces based

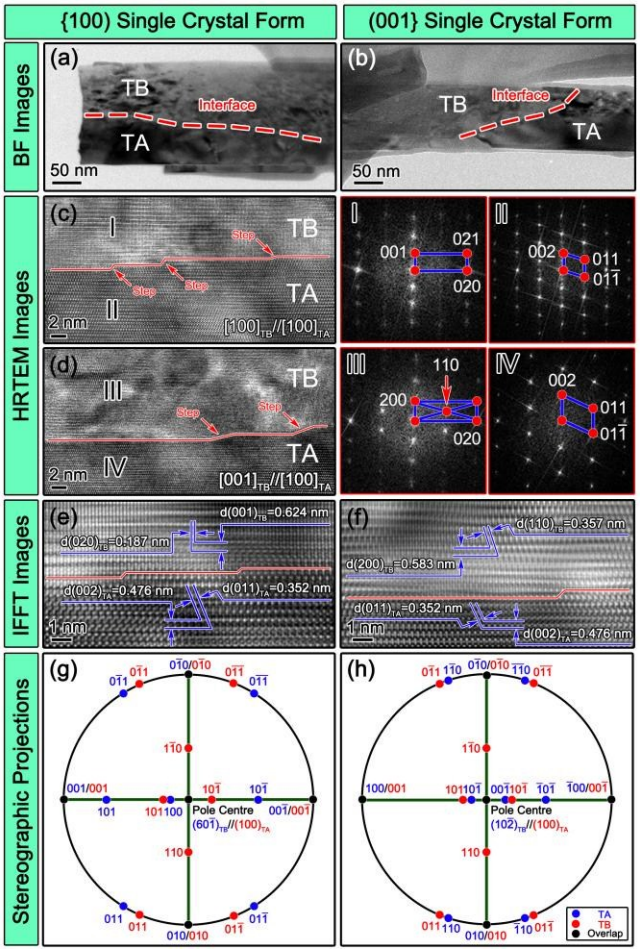

Fig. 4 The TEM BF images showing the curved interface structures for $\{100\}$ (a) and $\{001\}$ (b) SCF respectively. HRTEM figures (c) and (d) illustrate two types of ORs for the two SCFs. Meanwhile, the steps on the interfaces illustrated in the IFFT images for both SCFs (e) and (f) suggest the typical diffusional phase transformation process. The detailed crystallographic features for the two ORs are drawn in the stereographic projections of planes (g) and (h). Both ORs reveal an excellent crystallographic symmetry with (010) plane keeps overlapping.

on $(001\}$ SCF has already been reported in our previous research works.[24] Based on the TEM results, the stereographic projection of planes were drawn and shown in Fig. 4 (g) and (h) to illustrate the detailed ORs for both interfaces. The pole centers were set to be $(60\bar{1})_{TB}//(100)_{TA}$ and $(10\bar{2})_{TB}//(100)_{TA}$ for $\{100\}$ and $\{001\}$ SCF respectively, which were also considered to be the first lattice correspondence between TB and TA. Here $(60\bar{1})_{TB}$ and $(10\bar{2})_{TB}$ correspond to the normal plane of $[100]$ and $[001]$ directions respectively. The blue, red and black spots represent the lattice planes for TB, TA and overlapping spots respectively. For both ORs, the second lattice correspondence is $(010)_{TB}//(010)_{TA}$ according to Eq. (2). Under this conditions, the third lattice correspondence which perpendicular to the first two can be identified as $(001)_{TB}//(001)_{TA}$ and $(100)_{TB}//(001)_{TA}$ for $\{100)$ and $(001\}$ SCF respectively. Based on the lattice correspondence from the 3 basal axes, the detailed crystallographic OR can be projected. As seen from the Fig. 4 (g) and (h), both ORs show an excellent crystallographic symmetry, suggesting a lower strain for the lattice correspondence.

4. Discussions

4.1 The competition between $(001\}$ and $\{100)$ SCF in TB nanofibers.

The selection of SCFs normally happens during the nuclei and growth process and, definitely, will be affected by crystal growth environment such as temperature, concentration of solution and pressure. However, once these parameters are determined, the only factor which may influence the competition of SCF is the geometry factors, that is, the crystallographic structure and symmetry. Therefore, a simplified calculation based on the geometry factors has been carried out to interpret the competition mechanism of the two SCFs. To perform the calculation, 4 parameters which closely associate with the lattice planes were taken into consideration:

1. Lattice spacing (d_{hkl}). The d-spacing is an important index to consider the importance of a certain lattice plane. Normally, planes with larger values of d_{hkl} have lower growth speed and greater possibilities to be the slip plane of dislocations. Moreover, it is known that the lattice planes with a large d-spacing can be regarded as the close-packed plane or at least fairly close-packed.[30]

2. Multiplicity factor (P). The multiplicity factor is the impact factor of equivalent plane numbers on the diffraction intensities. Larger P value suggests more equivalent planes included in a certain lattice plane with miller index of (hkl).

3. Lorentz-polarization factor (φ (ϑ)). The Lorentz-polarization factor is also known as the angle factor. As a function of the diffraction angle (ϑ), this parameter reflects the differences of scattering intensity of atoms and cells along different directions. The factor can be calculated as follows:

$$\varphi(\theta) = \frac{1+\cos^2 2\theta}{\sin^2 \theta cos\theta} \quad (3)$$

4. Energy factor (E_{hkl}). The energy factor reflects the energy values of different lattice planes. If a plane does not contain or cut through any bond in the crystal lattice, then it can be defined as the "ground state". A positive value "s" will be used to represent the status. For a plane contain or cut through the bonds between anion and cation, the weight ratios are set to be 0.5 and 1 respectively. For example, if a lattice plane contain 4 bonds and cut through 2 bonds at the same time, then the energy factor should be $2s/(4\times2)=s/4$. For the special situation that only 1 bond is cut through or falls on a certain lattice plane, the weight ratio is set to be 1.5 to distinguish from the ground state. The more bonds are included or cut by a certain lattice plane, the larger growth speed is likely to present on the corresponding plane.

By multiply the 4 parameters together, a list represents the importance of different lattice planes can be obtained. The calculation results for (001) and (100) of TB are summarized in Table 2. The product column in the table indicates the product of the four factors listed above. Considering this column in the table, it is noted that (100) plane, which have a larger values of d-spacing and angle factor, ranked front than (001) plane although the energy factor of (100) is only one quarter than that of (001), indicating (100) SCF has a larger chance to win the competition. In fact, for the situation of diffraction in real lattice, (100) is forbidden due to the zero

value of structure factor. The (200) plane is found to have the similar diffraction intensity and structure factor with (001), suggesting the similar importance. However, the drop of the index would double the d-spacing and diffraction angle, leading to the significant increase of the importance. Also, the growth speed of (100) plane is likely to be lower than (001) due to its larger d-spacing according to Bravais' Law. Therefore, most of the nanofibers remain to be $\{100\}$ SCF due to the lower growth speed of (100) plane in our experiment.

4.2 The potential effect of multiple interfaces on the lithium ion transport properties.

As two types of TB/TA interfaces which are induced by the different TB SCFs coexisted, it is essential to understand the differences between these two types of interfaces from the perspective of lithium ion transport. As mentioned above, dual-phase interfaces are detrimental to the transport of lithium ions under normal circumstances. With different interface structures, the size of nanotunnels may vary across the interfaces, leading to the formation of different pathways. In this case, the crystal models of the two types of interface structures have been drawn to interpret the mechanism, as shown in Fig. 5 (a)-(d). For each SCF, two projection directions were chosen to illustrate both nanotunnels and interface coherency. According to the TEM results, the interfaces for $\{100\}$ and $(001\}$ SCFs are parallel to $(001)_{\mathrm{TB}}$ and $(100)_{\mathrm{TB}}$ respectively. Meanwhile, the growth directions of the nanofibers are found along $[010]_{\mathrm{TB}}$ for both SCFs. According to the previous results, the lowest energy lithium site is a slightly off-center position in the b-axis channel for low lithium concentration (x<0.125 for Li_xTiO_2-B). In addition, low Li migration energies are also found for pathways along b-axis channel.[21] Therefore, for the observation of nanotunnels in TB, the viewing directions were set to be $[010]_{\mathrm{TB}}//[010]_{\mathrm{TA}}$ for both SCFs, as shown in Fig. 5 (a) and (c). The interfaces between TB and TA are shown by yellow dashed lines.

The biggest nanotunnel located at the center of TB is the main and most effective one. It is also noticed that TB has larger size nanotunnels than TA, which is consistent with its excellent lithium ion transport properties. Although the interfaces observed from the direction of $[010]_{\mathrm{TB}}//[010]_{\mathrm{TA}}$ do not show an excellent coherent status, the nanotunnels at the centers of interfaces are all expanded for both SCFs. As the most suitable pathway for lithium ions is moving along $[010]_{\mathrm{TB}}$, which is the same with the growth direction of TB nanofibers, the interface here will not block the movement of lithium ions. Instead, the expansion of tunnels may allow more ions to pass at the same time, suggesting an increase of transport efficiency. In addition, the $(001\}$ SCF is found to have larger expanded tunnels and regular shaped interfaces, indicating a more suitable pathway than $\{100)$ SCF. Therefore, it is a possible effective way to enhance the lithium ion insertion properties by controlling the growth of TB nanofibers with $(001\}$ SCF.

According to the TEM results shown in Fig. 4, the interfaces of TB/TA show a great coherent state. Therefore, the interface models with the viewing directions of $[100]_{\mathrm{TB}}//[100]_{\mathrm{TA}}$ and $[001]_{\mathrm{TB}}//[100]_{\mathrm{TA}}$ (the same with TEM results) are also drawn in Fig. 5 (b) and (d). Seeing from the figure, it is found that both interfaces are fully coherent under this viewing direction. In addition, the nanotunnels of $(001\}$ SCF are larger than that of $\{100)$ SCF, consistent with the results from Fig. 5 (b) and (d). Considering the previous reports, low migration energy (~0.5 eV) along the direction of $[001]_{\mathrm{TB}}$ is confirmed besides the optimized b-axis pathway in TB structure.[21] This is another evidence to show that the nanofibers with $(001\}$ SCF have

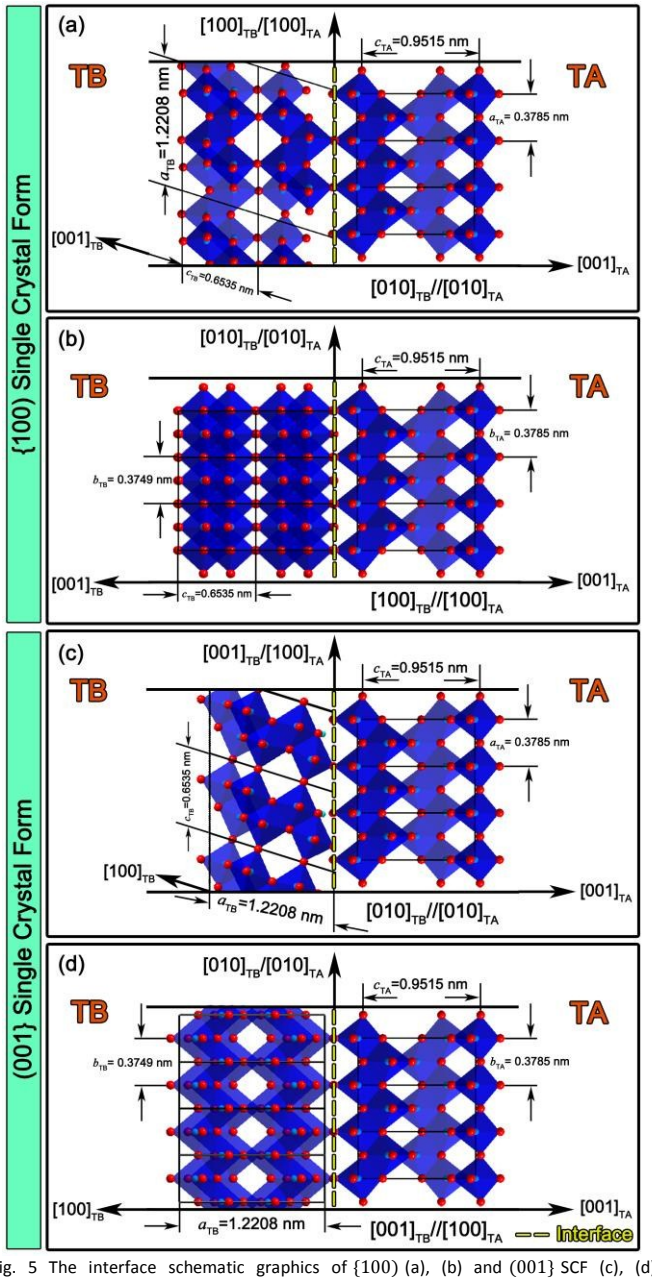

Fig. 5 The interface schematic graphics of $\{100)$ (a), (b) and $(001\}$ SCF (c), (d) respectively. Each SCF has two projection directions to illustrate the structures of nanotunnels and interface coherency. Both SCFs exhibit coherent interface structures when viewing along the same zone axes with the TEM results. Also, the $(001\}$ SCF shows larger nanotunnels expansion and less dangling bonds at the interface area (c) when compare with $\{100)$ SCF (a) when viewing along $[010]_{\mathrm{TB}}//[010]_{\mathrm{TA}}$ direction, indicating possible higher lithium ion transport efficiency for the TB nanofibers with $(001\}$ SCF.

Table 2 The calculation results for $(\mathbf{001})$ and $(\mathbf{100})$ planes in TB

(hkl)	d_{hkl} (nm)	P	2θ	ϕ (θ)	E_{hkl}	Product	Rank	Quantity	Diameter
(001)	0.6237	2	14.188	128.1756	s	159.89s	2	Less	Smaller
(100)	1.1652	2	7.598	452.6011	s/4	263.69s	1	More	Larger

better lithium ion transport properties.

4.3 Controlled synthesis of nanofibers with certain SCF

The researches on the controlled synthesis of metal-oxides nanocrystals with specific exposed facets are somewhat abundant recently.[31-34] Crystallographically, the nanocrystals with different facets normally belong to different SCFs. For certain nanocrystals, the competition between different SCFs is often existed during the crystal growth process. If the dominant facets are unwanted, the common method is to dope some elements to replace the atoms at the wanted planes to limit the growth rate. This method has been proved to be effective during the growth of anatase nanocrystals with certain facets.[34] The most available anatase crystals are dominated by the thermodynamically stable facets $\{101\}$ (more than 94 per cent, according to the Wulff construction).[35] That is, $\{101\}$ SCF wins the competition during the growth procedure. In fact, (101) in anatase has the largest diffraction intensity and lattice plane density no matter considering Bravais lattice or real lattice. However, the most reactive facet in anatase has been proved to be $\{001\}$, which has the diffraction intensity five times lower than that of (101) (considering the plane of (004)).[35-37] In this case, fluorine was added during the growth process to replace some oxygen atoms at the surface, leading to the fluorine-terminated surfaces with reversed priority.[34] For the situation of TB, the controlled synthesis of nanocrystals with certain SCF may easier as the importance difference between the first and second ranked planes is not as large as that of anatase. Further investigations may be needed to find out the elements which are suitable to dope into TB for the selection of different SCFs.

5. Conclusions

In summary, the morphology and competition mechanism of TB nanofibers with two types of SCFs were investigated in detail. The lath shape morphology for the two SCFs was confirmed through SEM observation and the thickness mapping technique. Moreover, by precisely determine the type of SCFs, TB nanofibers with $\{100\}$ main facets have been confirmed to be dominant. By calculating 4 crystallographic parameters, the competition mechanism between different SCFs was successfully interpreted. Furthermore, the TB/TA interfaces with different ORs have been produced and analyzed in detail. Both interfaces reveal fully coherent status with different crystallographic ORs. Moreover, $\{001\}$ SCF is found to have larger nanotunnels at TB/TA interface region, indicating a better lithium ion pathway. The controlled synthesis of TB nanofibers with certain SCF is also prospected at last.

Acknowledgements

The authors acknowledge the facility use and scientific and technical assistance from AMMRF at the University of Sydney. Z. L. wishes to thank the Australian Research Council for funding support (DP130104231).

Notes and references

† The close parenthesis and open brace represent the multiplicity of plane indexing. The symbol $(001\}$ indicate the combination between only (001) and $(00\bar{1}\}$. Situations are similarly to $\{100)$.

1. A. L. Linsebigler, G. Lu and J. T. Yates Jr, *Chemical reviews*, 1995, **95**, 735-758.
2. S. G. Kumar and L. G. Devi, *The Journal of Physical Chemistry A*, 2011, **115**, 13211-13241.
3. L. Liu and X. Chen, *Chemical reviews*, 2014, **114**, 9890-9918.
4. X. Chen and S. S. Mao, *Chemical reviews*, 2007, **107**, 2891-2959.
5. P. Roy, D. Kim, K. Lee, E. Spiecker and P. Schmuki, *Nanoscale*, 2010, **2**, 45-59.
6. Y.-B. Tang, C.-S. Lee, J. Xu, Z.-T. Liu, Z.-H. Chen, Z. He, Y.-L. Cao, G. Yuan, H. Song and L. Chen, *Acs Nano*, 2010, **4**, 3482-3488.
7. S. T. Myung, N. Takahashi, S. Komaba, C. S. Yoon, Y. K. Sun, K. Amine and H. Yashiro, *Advanced Functional Materials*, 2011, **21**, 3231-3241.
8. K. Liu, M. Cao, A. Fujishima and L. Jiang, *Chemical reviews*, 2014, **114**, 10044-10094.
9. R. V. Mikhaylov, A. A. Lisachenko and V. V. Titov, *The Journal of Physical Chemistry C*, 2012, **116**, 23332-23341.
10. D. O. Scanlon, C. W. Dunnill, J. Buckeridge, S. A. Shevlin, A. J. Logsdail, S. M. Woodley, C. R. A. Catlow, M. J. Powell, R. G. Palgrave and I. P. Parkin, *Nature materials*, 2013, **12**, 798-801.
11. B. Liu, A. Khare and E. S. Aydil, *ACS applied materials & interfaces*, 2011, **3**, 4444-4450.
12. A. G. Dylla, G. Henkelman and K. J. Stevenson, *Accounts of chemical research*, 2013, **46**, 1104-1112.
13. A. G. Dylla, P. Xiao, G. Henkelman and K. J. Stevenson, *The Journal of Physical Chemistry Letters*, 2012, **3**, 2015-2019.
14. Y. V. Kolen'ko, K. A. Kovnir, A. I. Gavrilov, A. V. Garshev, J. Frantti, O. I. Lebedev, B. R. Churagulov, G. Van Tendeloo and M. Yoshimura, *The Journal of Physical Chemistry B*, 2006, **110**, 4030-4038.
15. J. Cai, Y. Wang, Y. Zhu, M. Wu, H. Zhang, X. Li, Z. Jiang and M. Meng, *ACS applied materials & interfaces*, 2015, **7**, 24987-24992.
16. D. Tsukamoto, Y. Shiraishi, Y. Sugano, S. Ichikawa, S. Tanaka and T. Hirai, *Journal of the American Chemical Society*, 2012, **134**, 6309-6315.

17. J. Liu, H. Bai, Y. Wang, Z. Liu, X. Zhang and D. D. Sun, *Advanced Functional Materials*, 2010, **20**, 4175-4181.
18. A. Takai and P. V. Kamat, *Acs Nano*, 2011, **5**, 7369-7376.
19. D. Hu, W. Zhang, Y. Tanaka, N. Kusunose, Y. Peng and Q. Feng, *Crystal Growth & Design*, 2015, **15**, 1214-1225.
20. R. Kaplan, B. Erjavec, G. Dražić, J. Grdadolnik and A. Pintar, *Applied Catalysis B: Environmental*, 2016, **181**, 465-474.
21. C. Arrouvel, S. C. Parker and M. S. Islam, *Chemistry of Materials*, 2009, **21**, 4778-4783.
22. H. Liu, Z. Zheng, D. Yang, X. Ke, E. Jaatinen, J.-C. Zhao and H. Y. Zhu, *Acs Nano*, 2010, **4**, 6219-6227.
23. D. Yang, H. Liu, Z. Zheng, Y. Yuan, J.-C. Zhao, E. R. Waclawik, X. Ke and H. Zhu, *Journal of the American Chemical Society*, 2009, **131**, 17885-17893.
24. Y. Lei, J. Sun, H. Liu, X. Cheng, F. Chen and Z. Liu, *Nanoscale*, 2014, **6**, 14237-14243.
25. V. Pfeifer, P. Erhart, S. Li, K. Rachut, J. Morasch, J. Brötz, P. Reckers, T. Mayer, S. Rühle and A. Zaban, *The Journal of Physical Chemistry Letters*, 2013, **4**, 4182-4187.
26. Y. Mi and Y. Weng, *Scientific reports*, 2015, **5**, 11482.
27. H. Zhu, X. Gao, Y. Lan, D. Song, Y. Xi and J. Zhao, *Journal of the American Chemical Society*, 2004, **126**, 8380-8381.
28. Y. Lei, J. Sun, H. Liu, X. Cheng, F. Chen and Z. Liu, *Chemistry-A European Journal*, 2014, **20**, 11313-11317.
29. Q. Wang, Z. Wen and J. Li, *Advanced Functional Materials*, 2006, **16**, 2141-2146.
30. P. Kelly, H.-P. Ren, D. Qiu and M.-X. Zhang, *Acta Materialia*, 2010, **58**, 3091-3095.
31. M. Liu, L. Piao, L. Zhao, S. Ju, Z. Yan, T. He, C. Zhou and W. Wang, *Chemical Communications*, 2010, **46**, 1664-1666.
32. X. Han, Q. Kuang, M. Jin, Z. Xie and L. Zheng, *Journal of the American Chemical Society*, 2009, **131**, 3152-3153.
33. M. Leng, M. Liu, Y. Zhang, Z. Wang, C. Yu, X. Yang, H. Zhang and C. Wang, *Journal of the American Chemical Society*, 2010, **132**, 17084-17087.
34. H. G. Yang, C. H. Sun, S. Z. Qiao, J. Zou, G. Liu, S. C. Smith, H. M. Cheng and G. Q. Lu, *Nature*, 2008, **453**, 638-641.
35. M. Lazzeri, A. Vittadini and A. Selloni, *Physical Review B*, 2001, **63**, 155409.
36. A. Vittadini, A. Selloni, F. Rotzinger and M. Grätzel, *Physical Review Letters*, 1998, **81**, 2954.
37. Y.-w. Jun, M. F. Casula, J.-H. Sim, S. Y. Kim, J. Cheon and A. P. Alivisatos, *Journal of the American Chemical Society*, 2003, **125**, 15981-15985.

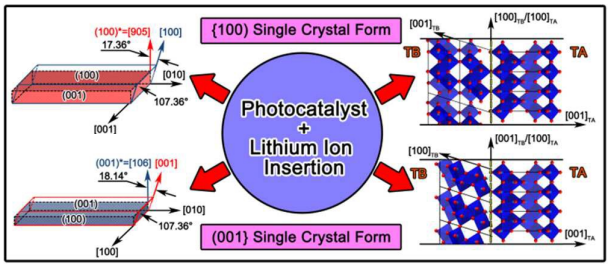

Two types of TiO_2 (B) single crystal forms as well as the induced TiO_2 (B)/anatase interfaces in one nanofiber with different orientation relationships are well studied with the aim of multi-purpose nanofiber synthesis. TiO_2 (B) fibers with $\{001\}$ single crystal form are confirmed to reveal larger nanotunnels, which is speculated to enhance the passing rate of Li^+ ions though the quantity is not dominant. In addition, the interfaces with two orientation relationships exhibit fully coherent status which will definitely improve the photocatalytic performance for the dual-phase nanofibers.